Nanoscale

Accepted Manuscript

This article can be cited before page numbers have been issued, to do this please use: S. Choyal, B. S. A. Gedara, A. Ologun, L. Li, M. Trenary and N. Jiang, *Nanoscale*, 2026, DOI: 10.1039/D6NR00871B.

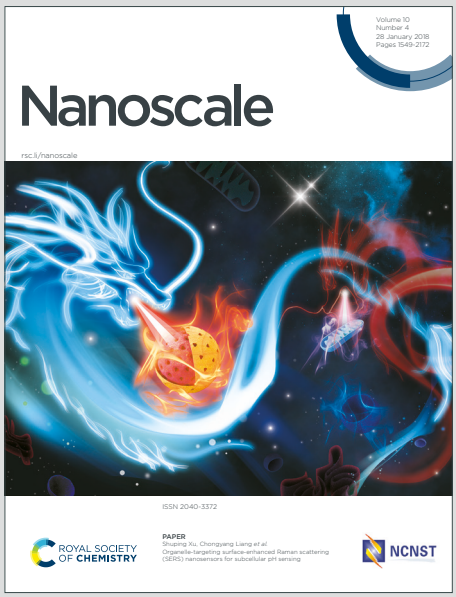

ROYAL SOCIETY OF CHEMISTRY

rsc.li/nanoscale

View Article Online
DOI: 10.1039/D6NR00871B

ARTICLE

Templated Growth and Intercalation Pathways of Nickel Nanoclusters on Graphene/Ir(111)

Received 00th January 20xx,
Accepted 00th January 20xx

DOI: 10.1039/x0xx00000x

Shilpa Choyal,[a] Buddhika S. A. Gedara,[a] Ayoyele Ologun,[a] Linfei Li,[a] Michael Trenary,[a] and Nan Jiang*[a, b]

The growth and intercalation of nickel (Ni) nanoclusters on the moiré superlattice of graphene(Gr)/Ir(111) were investigated by scanning tunneling microscopy (STM) under ultra-high vacuum (UHV) conditions. At room temperature (RT), Ni deposition led to the formation of flat, triangular islands, with nucleation preferentially occurring at fcc regions of the moiré superlattice. These islands evolved into three-dimensional triangular nanoclusters that were aligned with the substrate's close-packed directions, reflecting the templating effect of the graphene moiré. Upon annealing to 900 K, Ni atoms intercalated beneath the graphene layer, yielding two distinct moiré contrasts signifying different local intercalation configurations. These findings demonstrate that Ni nanostructures confined by the moiré template provide a well-defined platform for exploring size- and shape-dependent properties relevant to catalytic and magnetic applications.

1. Introduction

Metallic clusters, particularly those of transition metals, possess unique catalytic and magnetic properties. When reduced to nanometer dimensions, these clusters exhibit quantum size effects[1,2] and unusual chemical reactivity,[3] leading to novel electronic structures,[4,5] magnetic properties,[6,7] and size-dependent catalytic activities.[6] These distinctive properties make transition metal nanoclusters promising candidates for applications in heterogeneous catalysis,[8] spintronics,[7] and nanoelectronics applications.[8] To this end, the ability to control their size and arrangement is critical for optimizing their performance in these fields. Among the various methods utilized for synthesizing ordered nanocluster arrays,[8,9] the bottom-up strategy of templated self-organization stands out as particularly promising. Using this approach, metal nanoclusters with precisely controlled size and arrangement are obtained via direct deposition of metal atoms onto the ordered rippled thin film grown on a metal crystal substrate. Transition metal substrates both catalyze and template graphene growth, providing an ideal platform for controlled single-layer formation.[5,9,10] The lattice mismatch between graphene and the underlying substrate generates moiré superstructures that create periodic binding sites for adatoms and small clusters. Recent studies demonstrate the formation of ordered nanocluster arrays on graphene moiré patterns on various close-packed metal surfaces, including Pt(111),[11,12] Rh(111),[11,13] Ru(0001),[11,14,15] and Ir(111).[11,16–18] Notably, well-ordered superlattices of metallic clusters comprising Re, W, Pt, and Ir on these templates have also been fabricated.[19–21] The degree of ordering, preferred nucleation sites, and thermal stability of the clusters depend sensitively on the interplay between metal–carbon interaction strength, metal cohesive energy, and growth kinetics.[20] Intercalation phenomena add further complexity, as metals such as Hf,[22] Fe,[23] Cu,[24] and Pb[25] migrate beneath graphene at elevated temperature, decoupling graphene from the substrate and often restoring its intrinsic electronic properties.

Despite recent advances in moiré-templated nanocluster studies, the behavior of nickel nanoclusters on graphene remains largely unexplored. Nickel offers a particularly compelling system because of its importance in heterogeneous catalysis and spintronics. Studies on Ni/Gr/Rh(111) have shown that room-temperature deposition produces triangular nanoclusters templated by the moiré pattern.[13] Although deposition at 150 K produces monodispersed clusters, increasing the coverage prevents the establishment of long-range ordering.[13] In contrast, graphene on Ir(111) couples more weakly to the substrate than on Rh(111) and forms a highly uniform moiré superstructure, providing a more robust platform for stabilizing ordered Ni nanoclusters and exploring their intercalation behavior. Nevertheless, systematic studies of Ni on Gr/Ir(111), particularly those addressing its thermal stability and intercalation have not been reported, revealing a significant gap in the literature.

[a] Department of Chemistry, University of Illinois Chicago, 845 West Taylor Street, Chicago, Illinois 60607, United States
[b] Department of Physics, University of Illinois Chicago, 845 West Taylor Street, Chicago, Illinois 60607, United States

Supplementary Information available: [details of any supplementary information available should be included here]. See DOI: 10.1039/x0xx00000x

In this study, we address this gap by investigating the growth dynamics and intercalation behavior of nickel on Gr/Ir(111) using scanning tunneling microscopy (STM) and low-energy electron diffraction (LEED). At room temperature, we observe the formation of triangular-shaped nickel nanoclusters precisely registered by the graphene moiré pattern. Upon annealing at 900 K, Ni intercalates beneath the graphene layer, generating inverted moiré contrasts while preserving the periodicity, consistent with pseudomorphic Ni growth on Ir(111). These results advance our fundamental understanding of metal–graphene interactions and establish Ni/Gr/Ir(111) as a model system for studying templated cluster growth and thermally driven intercalation, with potential implications for catalysis, spintronics, and graphene-based device engineering.

2. Experimental Methods

The experiments were performed in an ultra-high vacuum (UHV) chamber with a base pressure of ~1 × 10^{-10} Torr. STM topographic images were obtained at room temperature (RT) with an Omicron, GmbH, variable-temperature scanning probe microscope (VT-SPM) system. Images were acquired with Omicron MATRIX software, and data processing was done with the WSxM program provided by Nanotech.[26] The Ir(111) single crystal was purchased from Surface Preparation Laboratory with 99.995% purity, orientation accuracy ~0.1˚, top surface polished to a roughness < 0.03 µm, 6 mm in diameter, and 1 mm in height. The Ir(111) surface was cleaned by repeated cycles of sputtering with argon (3.5 × 10^{-5} Torr, 1000 V) and annealing to ~1500 K. A custom-designed e-beam heater was used to reach the required annealing temperature.[27] The crystal temperature was measured with an optical pyrometer based on an estimated emissivity of 0.1. The surface was verified to be clean by low-energy electron diffraction (LEED) and STM images (Figure S1). Graphene was prepared by exposing it to 15 Langmuir (2.5 × 10^{-8} Torr for 10 minutes) of ethylene at a crystal temperature of ~1200 K, followed by annealing to ~1500 K for 2 minutes. Nickel was deposited on the graphene layer via evaporation from a pure Ni rod (Goodfellow, 99.95%) by a triple electron beam evaporator (EFM 3T). During Ni evaporation, samples were held at RT, and the Ni coverage from STM was determined by depositing Ni on Ir(111) and analyzing large area images collected from different regions of the surface. We generated cluster size histograms by evaluating multiple STM images acquired from distinct areas of the crystal.

3. Results and Discussion

3.1. Graphene on Ir(111)

Large, atomically flat graphene-covered terraces extending several hundred nanometers were observed in scanning tunneling microscopy (STM) images (Figure 1a), indicating continuous and homogeneous graphene coverage across step edges. The absence of uncovered regions and the “carpet-like” growth mode reflect the high crystalline quality of the

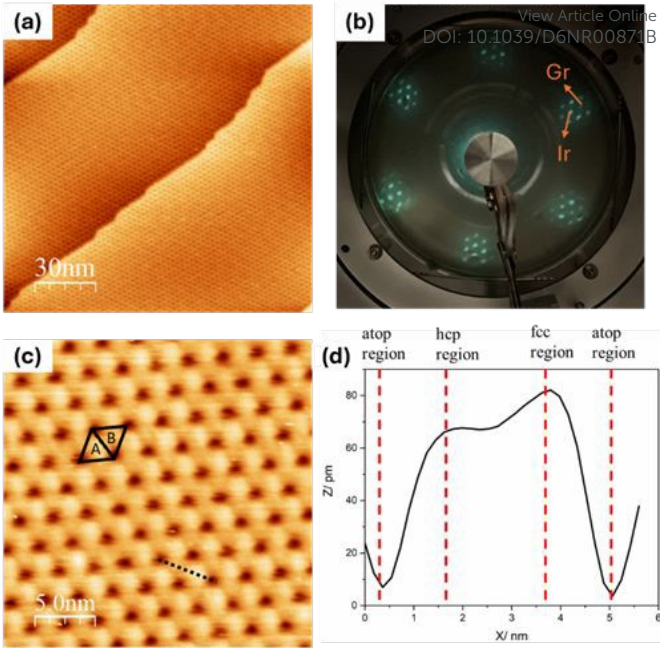

Figure 1. (a) STM image showing continuous graphene growth across multiple Ir step edges. Scanning parameter: I = 1200 pA, V = −0.6 V. (b) Corresponding LEED pattern recorded at 70 eV, displaying the hexagonal diffraction spots of both graphene and Ir(111), together with satellite spots arising from the moiré superstructure. (c) High-resolution STM topograph highlighting the periodic moiré pattern with a periodicity of 2.5 ± 0.2 nm. The moiré unit cell is outlined by a black rhombus, with fcc and hcp regions marked by A and B, respectively. Scanning parameter: I = 600 pA, V = +1 V. (d) Line profile taken along the dashed black line in (c), comparing the apparent heights of atop, fcc, and hcp regions.

graphene, consistent with previous reports on epitaxial Gr/Ir(111). The structural schematic of Gr/Ir(111) is well established in the literature and is illustrated in Figure 2.[18] Only a small number of defects, primarily point vacancies and isolated edge dislocations accommodating small-angle tilt boundaries, were identified in high-magnification STM images (Figure S2).[17]

The macroscopic quality of the film was confirmed by LEED (Figure 1b). The hexagonal diffraction pattern exhibits two sets of spots corresponding to the Ir(111) substrate (inner) and the graphene overlayer (outer). Additional satellite spots arranged in hexagonal symmetry are clearly resolved, arising from the moiré superstructure. The measured moiré periodicity is 2.5 ± 0.2 nm, in agreement with the reported value of 2.52 nm.[18,19,22] This superlattice is also resolved in a high-resolution STM image (Figure 1c), where a rhombic unit cell highlights the periodic corrugation. A line profile (Figure 1d) across the moiré unit cell reveals three distinct high-symmetry registry positions between the graphene and the underlying Ir lattice: atop, fcc, and hcp sites. Atop regions occur when the centers of graphene hexagons are positioned directly above Ir atoms and typically appear as depressions in STM images. However, this contrast is sensitive to imaging conditions and can vary depending on the polarity and the electronic structure of the tip during scanning.[18] In contrast, fcc and hcp regions correspond to hollow-site registries, where the hexagon centers lie above

View Article Online
DOI: 10.1039/D6NR00971B

threefold sites on the Ir(111) surface. The fcc and hcp sites differ by their stacking sequence relative to the second-layer Ir atoms.

Taken together, these results confirm the successful preparation of large-area, high-quality monolayer graphene on Ir(111), exhibiting a well-defined moiré superstructure with atop, fcc, and hcp adsorption sites. The weak but spatially modulated interaction between graphene and Ir(111) establishes this system as an ideal platform for studying site-selective adsorption, intercalation processes, and templated nanocluster growth.

3.2. Templated growth of Ni on Gr/Ir(111)

To investigate Gr/Ir(111) as a template for metal nanocluster growth, Ni was deposited onto the Gr/Ir(111) surfaces at room temperature (RT). Figure 2(a) displays an STM image of 0.12 ML Ni deposited on large graphene terraces across Ir step edges. The surface is decorated with a few Ni nanoclusters, which adopt well-defined triangular morphologies with edges aligned preferentially along the $\langle 1\bar{1}0 \rangle$ crystallographic direction of the Ir(111) substrate. Despite the relatively weak Ni–graphene interaction, the underlying moiré pattern effectively directs both the positional order and orientational alignment of the triangular islands. The average apparent cluster height was approximately 1.4 ± 0.2 nm [Figures 2(b,c)] corresponding to about 6-7 atomic layers of Ni, with typical edge lengths of 6.3 ± 2.0 nm, extending across more than one moiré unit cell. The formation of large islands spanning multiple moiré cells indicates the significant surface mobility of Ni on graphene even at RT, consistent with prior observations of metal cluster growth on Gr/Rh(111).[13]

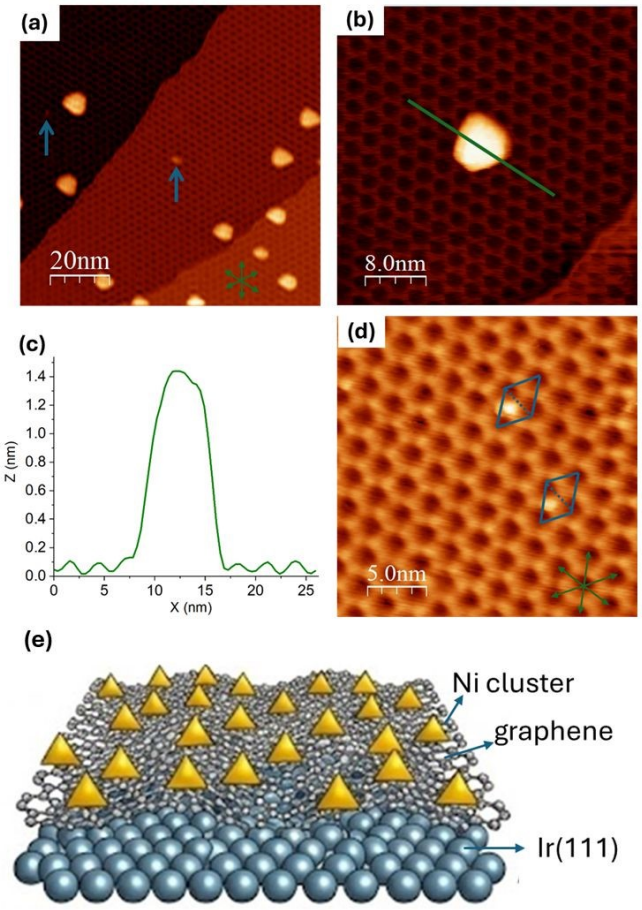

Figure 2. (a) STM image after deposition of 0.12 ML Ni showing the initial nucleation of small clusters (blue arrows). (b) STM image of a representative three-dimensional (3D) Ni nanocluster. (c) Line profile along the green line in (b), showing an apparent cluster height of ~1.4 nm. (d) Magnified STM image highlighting preferential nucleation of Ni nanoclusters at fcc regions of the graphene moiré pattern. The close packed direction of Ir(111) are indicated by the green arrows in the bottom right of (a,d). (e) Schematic illustration of Ni nanoclusters deposited at room temperature on the Gr/Ir(111) template. Scanning parameters: (a) V = +1.1 V, I = 200 pA; (b) V = +1.1 V, I = 200 pA; (d) V = −0.6 V, I = 1100 pA.

Further examination of the nucleation behavior reveals a strong preference for the fcc regions of the graphene moiré lattice. Quantitative analysis indicates that 77% of Ni nanoclusters nucleate at fcc sites and 23% at atop sites, with no nucleation observed at hcp sites (Figure S3). Consistent with this distribution, Figure 2(d) shows that nanoclusters predominantly occupy fcc sites. This site preference contrasts with that observed for other metals on Gr/Ir(111), such as Ir, Pt, W, and Re, which nucleate predominantly at the hcp regions.[19] In contrast, on Gr/Ru(0001), where graphene–metal bonding is significantly stronger and induces local rehybridization of sp^2 carbon to sp^3, nucleation instead occurs at fcc regions.[21,28] The fcc and hcp hollow sites on Gr/Ir(111) are geometrically equivalent due to the weaker graphene–Ir interaction compared to Ru and Rh, whereas the atop, fcc, and hcp sites remain electronically distinct.[29] In accordance with this observation, Li et al. demonstrated that Hf clusters populate both fcc and hcp moiré registries on Gr/Ir(111), but with a greater population on fcc sites.[26] In contrast, our results show that Ni clusters predominantly occupy fcc sites, with only a small fraction located at atop sites. This preference is attributed to the local rehybridization of graphene toward sp^3-like bonding upon Ni adsorption, which enhances the interaction at the fcc sites of the graphene moiré.[30,31]

We next investigated stepwise versus continuous deposition of Ni nanoclusters at RT (Figure 3). In stepwise growth, Ni exposures were performed sequentially to obtain coverages of 0.12, 0.5, and 0.9 ML. Here, the average island edge length increased gradually from 6.3 nm (0.12 ML) to 8.8 nm (0.5 ML) to 16.5 nm (0.9 ML), while the height changed from ~1.4 ± 0.2 nm to 1.6 ± 0.2 nm to 1.8 ± 0.2 nm (~8–9 atomic layers). In contrast, continuous deposition of 0.5 ML Ni produced larger triangular clusters averaging 10.3 nm in edge length with smoother top facets (Figure 3d). Morphology histograms [Figures 3(e,f)] highlight the differences: stepwise deposition leads to a broader size distribution and increasing shape irregularities, including truncated triangles and rounded islands, which is clearly reflected in sequential deposition (Figure S4), whereas nanocluster shapes become increasingly irregular as coverage increased from 0.12 to 0.9 ML, accompanied by a broadening in the cluster size distribution as shown in the histograms. In contrast, continuous growth yields a narrower size distribution with well-defined triangular shapes. This behavior mirrors prior studies of Dy/Gr, where continuous deposition produced smooth multi-height triangular fcc(111)

View Article Online
DOI: 10.1039/D6NR00871B

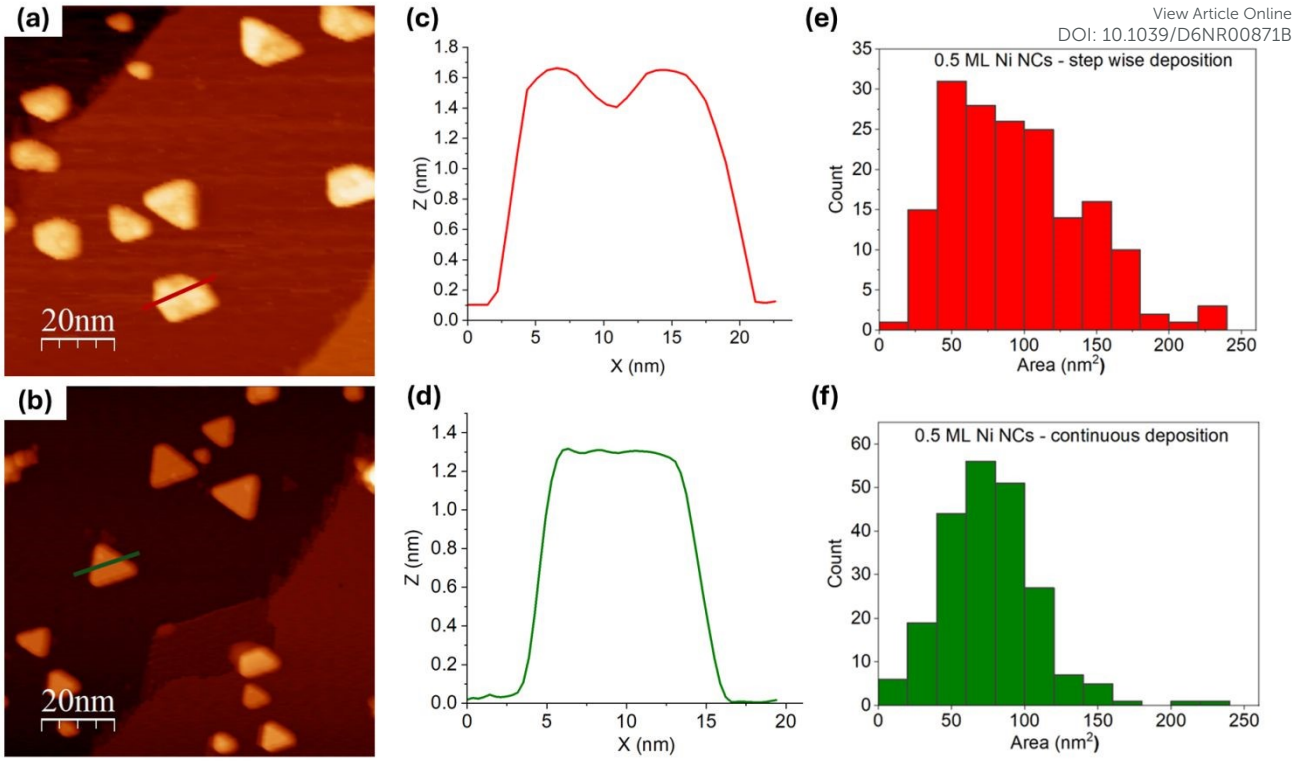

Figure 3. Comparison of stepwise and continuous Ni nanocluster growth on Gr/Ir(111) at RT. (a) STM image of 0.5 ML of Ni obtained by stepwise deposition following an initial 0.12 ML seed layer, showing irregular triangular and truncated islands. (b) STM image of 0.5 ML Ni deposited directly in a single step, yielding well-defined triangular nanoclusters with flatter top facets. (c, d) Line profiles taken along the two different growth modes: stepwise (red line in (a)) and continuous (green line in (b)). These profiles highlight differences in cluster morphology. (e, f) Histograms of cluster area distributions corresponding to the stepwise (a) and continuous (b) growth modes. Stepwise deposition results in a broader size distribution, whereas continuous growth produces a narrower distribution with more uniform cluster sizes. Scanning parameters: (a) V = +2.0 V, I = 300 pA; (b) V = −0.9 V, I = 300 pA.

islands, whereas stepwise growth was kinetically limited, resulting in incomplete layers.[32]

The morphological divergence arises as a result of uphill diffusion, and Ostwald ripening, of Ni adatoms on the weakly interacting Gr/Ir(111) template. During stepwise deposition, adatoms ascend onto pre-existing islands before completing lower layers, yielding irregular or truncated shapes, whereas under continuous deposition, the system relaxes toward the thermodynamically favored triangular morphology. Line profile (Figure 4b) shows that second-layer nucleation occurs predominantly at island edges in continuous growth but shifts to mixed edge- and center-nucleation when deposition is interrupted. Microscopically, an Ehrlich–Schwoebel (ES) barrier suppresses downward hopping, trapping adatoms on island tops and funneling them to edges,[33] where higher coordination at step and corner sites lowers the critical nucleus formation energy. This is consistent with first-principles studies of Pt nanoclusters on graphene moiré superlattices by Zhou et al., which showed that nucleation at highly coordinated configurations is energetically favored.[29] Growth interruptions allow thermal ripening, edge straightening, strain redistribution, diminishing edge reactivity, and flattening the energetic landscape across the island. Upon resuming deposition, enhanced adatom mobility and a reduced edge driving force permit interior nucleation. Collectively, these results underscore that the balance between ES-mediated kinetics and thermally driven relaxation controls second-layer registry and island symmetry in Ni/Gr/Ir(111).

Overall, these results establish that Ni forms triangular, multilayer islands on Gr/Ir(111) at RT, with nucleation mostly confined to the fcc moiré sites and morphology strongly dependent on the growth mode. The triangular islands resemble those observed for Dy/Gr, where anisotropic corner-crossing kinetics favor triangular shapes over hexagons.[32] The interplay between template registry, surface mobility, and deposition mode highlights the delicate balance of kinetic and

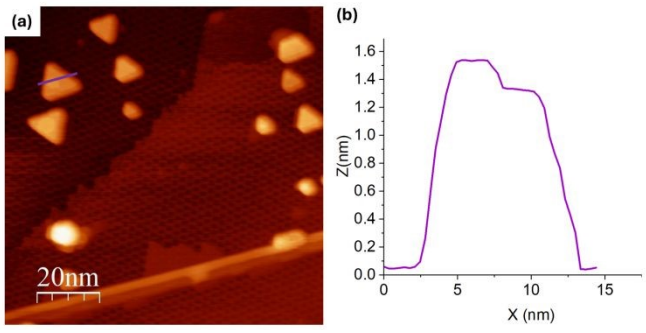

Figure 4. Edge-selective growth of Ni nanoclusters on Gr/Ir(111) at RT. (a) STM image of 0.5 ML Ni deposited continuously, showing triangular nanoclusters with well-defined edges. (b) Line profile along the purple line in (a), indicating preferential nucleation of the subsequent Ni layer at the island edges. Scanning parameters: V = −0.6 V, I = 300 pA.

thermodynamic factors governing nanocluster growth on weakly interacting Gr/metal substrates. Hence, such ordered Ni nanoclusters may serve as model systems for probing site-specific catalytic reactivity or for engineering spin-dependent properties in graphene-based nanostructures.

3.3. Intercalation of Ni between Gr and Ir(111)

To probe Ni intercalation at moderate temperature, an as-deposited 0.9 ML Ni film on Gr/Ir(111) was annealed to 900 K. Upon annealing, all 3D Ni clusters disappeared from the surface. Instead, STM images [Figure 5(a, b)] revealed a new moiré contrast, indicating that this temperature is sufficient to drive essentially all Ni atoms beneath the graphene layer. Following Ni intercalation, the graphene moiré becomes clearly visible with inverted contrast while retaining the same periodicity as pristine Gr/Ir(111). Small patches with different heights are observed (Figure 5 and Figure S5), corresponding to regions containing intercalated monolayer Ni islands beneath graphene, in contrast to bare Ir(111) terraces. This contrast inversion originates from Ni atoms intercalated beneath graphene at specific adsorption sites, which modifies the local electronic structure probed by STM.

Although the overall moiré periodicity remains unchanged upon Ni intercalation, the STM moiré contrast becomes significantly more complex. On some terraces, a "round" moiré pattern (Figure 5a) is observed with the same periodicity as pristine Gr/Ir(111), whereas other regions display a distinctive "clover-like" pattern (Figure 5b). In the round-pattern regions, each moiré unit cell shows a single protrusion (dot) located at the site that corresponds to a depression on the pristine Gr/Ir(111). In contrast, the clover-like regions exhibit a multi-lobed feature, indicating that Ni occupies multiple high-symmetry adsorption sites beneath the graphene layer. These observations demonstrate that Ni intercalates site-selectively within the moiré supercell.

Initially, Ni atoms preferentially migrate beneath the most energetically favored sites (mainly fcc, with some atop) of the graphene moiré superlattice, resulting in a round moiré contrast. After these sites are saturated, additional Ni atoms populate secondary preferred configurations, giving rise to a clover-like moiré contrast, as indicated by white arrows in Figure 5b. With further increase in local Ni availability, Ni atoms start to occupy all three available moiré sites, leading to the formation of locally complete Ni monolayer islands beneath graphene, highlighted by blue arrows in Figures 5(a) and 5(b). At this stage, Ni adopts the in-plane lattice of Ir(111), resulting in pseudomorphic growth at the graphene-Ir interface and preserving the same moiré periodicity. Consequently, the "round" moiré pattern observed for a fully formed Ni layer is indistinguishable from that arising from intercalation at a single site based solely on STM images. This site-selective occupation is schematically illustrated in Figures 5(c–e) using a model adapted from Halle et al. for Li intercalation beneath graphene on Ir(111).[34] In certain regions, constrained diffusion of Ni atoms beneath graphene leads to locally higher Ni densities compared to surrounding areas. Under these conditions, a second Ni layer begins to intercalate, as evidenced by the reemergence of clover-like features along with round moiré contrasts on triangular islands. Upon the occupation of all three moiré sites in the second Ni layer, regions without a discernible moiré pattern emerge, as marked by white circles in Figure 5b. In regions where the intercalated Ni thickness exceeds one monolayer, the Ni film gradually relaxes toward the bulk Ni(111) lattice constant. As a result, the graphene–Ni lattice mismatch is reduced and the graphene moiré contrast becomes weaker or disappears locally, consistent with the behavior of graphene on bulk-like Ni(111).[35] Control experiments support this interpretation. When Ni is deposited directly on Ir(111) and annealed to 900–1500 K, no moiré pattern was observed; instead, Ni grew pseudomorphically on Ir(111). Annealing at 900 K yields predominantly 2D pseudomorphic Ni islands, with occasional nucleation of a second Ni layer on top (Figure S6a). At 1500 K, the Ni coverage decreases, resulting in well-defined single-layer truncated hexagonal Ni islands due to Ni desorption at the elevated temperature (Figure S6b).

This pseudomorphic Ni layer adopts the in-plane lattice of Ir(111), as evidenced by the persistence of the graphene moiré pattern with a periodicity of 2.5 nm (Figure S5), identical to that observed on bare Ir(111). More specifically, the intercalated Ni layer occupies fcc sites on Ir(111) and matches the (9×9) Ir unit

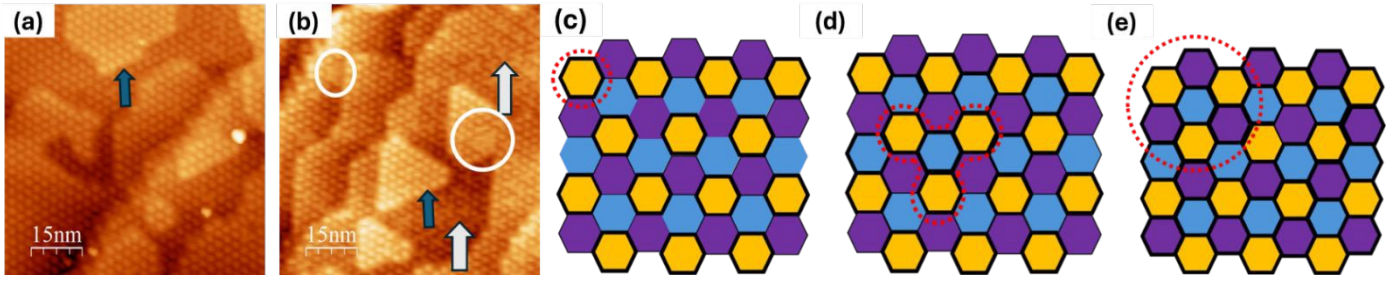

Figure 5. STM images after intercalation of Ni between graphene and Ir(111). (a, b) Two different scan areas showing distinct moiré contrasts: round and clover-like. The region in (b) exhibits a more clover-like contrast compared to (a); these clover-like features are marked by white arrows in (b). Blue arrows indicate islands where Ni occupies all three sites, forming a complete Ni monolayer beneath graphene. White circles highlight regions where second-layer Ni intercalation has initiated. The round moiré exhibits the same periodicity as that of Gr/Ir(111), indicating pseudomorphic growth of Ni on Ir(111). (c–e) Schematic representations of the moiré lattice, with colored hexagons denoting the three adsorption sites (fcc in yellow, hcp, and atop in blue and purple). Regions occupied by intercalated Ni assemblies are outlined by bold borders, giving rise to the round moiré contrast (c), the clover-like contrast (d), and the fully pseudomorphic Ni monolayer (e). The red dotted circle in (e) indicates regions where Ni occupies all three sites, consistent with the features marked by white circles in (b).

cell, which, in combination with the overlying graphene (10×10) supercell, reproduces the original moiré periodicity.[23] These findings are consistent with element-resolved studies of Fe intercalation in Gr/Ir(111), where XPD measurements showed that a single-layer Fe intercalant assumes the same in-plane lattice constant as Ir(111) (fcc stacking) while preserving the Gr (10×10)/Fe (9×9) supercell with a ~2.5 nm periodicity.[23] Despite the presence of these 2D intercalated islands, the underlying moiré periodicity remains intact, and only limited lateral coalescence is observed. This behavior aligns with graphene-mediated surfactant growth, where the graphene monolayer modulates Ni adatom diffusion and bonding. Consequently, Ni diffusion is confined within individual moiré cells, and the shape of the intercalated Ni islands is strongly guided by the moiré template rather than by isotropic growth. Similar mixed moiré contrasts are reported in other Gr/metal intercalation systems, suggesting that the moiré superlattice could serve as a template for the intercalant arrangement.[34,36] In our study, the coexistence of round and clover-like moiré domains likely reflects slight local variations in Ni coverage; however, the fundamental periodicity and symmetry of the lattice remain governed by the Gr–Ir registry.

The mechanism of Ni intercalation underneath graphene remains an active area of investigation, with several pathways proposed: (i) diffusion through graphene edges,[37–40] (ii) penetration via wrinkles or domain boundaries,[41–44] (iii) diffusion through point defects (e.g., atomic vacancies in the graphene lattice), which is very likely to occur for epitaxial graphene on metals, such as Gr/Ir(111), Gr/Ru(111), and Gr/Ni(111),[45–47] and (iv) an exchange intercalation mechanism, whereby transient metal-carbon bonding enables metal adatoms to slip beneath the graphene layer, followed by self-healing of the graphene lattice.[36,48] In the present case, pathways (i) and (ii) are unlikely, since intercalation occurs under a continuous, wrinkle-free graphene monolayer. Instead, the random spatial distribution of Ni islands (Figure S5) across the surface suggests contributions from (iii) and (iv) pathways. Epitaxial graphene on metal substrates such as Ir(111) typically contains some point defects, which can serve as local gateways for adatom intercalation. Furthermore, previous studies indicate that Ni atoms do not require extended defects to intercalate; rather, they can penetrate directly through the graphene lattice, in contrast to metals such as Pb, which rely on open edges or large defects.[25] In line with these findings, Ni intercalated beneath an otherwise intact graphene sheet at 900 K, suggesting either native point defects or a transient Ni-C mediated pathway.

In particular, an exchange-intercalation mechanism appears highly plausible for Ni. Such a mechanism would involve a Ni adatom first adsorbing on graphene and strongly binding to a carbon atom or a carbon–carbon (C–C) bond, thereby temporarily disrupting the graphene lattice. Density functional theory (DFT) calculations[49] and in situ microscopy studies by Bao and coworkers[25] have demonstrated that Ni intercalation in Gr/Ru(0001) is dominated by an exchange process of this kind. The Ni–C interaction is sufficiently strong to break a C–C bond, forming a transient Ni–C "bridge" state that allows the Ni atom to insert beneath the graphene layer, effectively displacing a carbon atom and bonding to the substrate below. Subsequently, the displaced carbon atom can reform the broken bond or reattach to a different location on the lattice, leaving the graphene layer with minimal permanent damage. Although the energy barriers for such processes are high, the thermal energy available at 900 K, together with the strong thermodynamic driving force for Ni to bond with Ir(111), can overcome these barriers. While a precise quantitative assessment would require dedicated density functional theory calculations, which are beyond the scope of the present work, estimates based on analogous graphene intercalation systems,[36,50] together with the annealing durations on the order of minutes suggest that sufficient thermal activation is available to drive intercalation. In addition, graphene's intrinsic flexibility and the mobility of defects at elevated temperatures can contribute to its self-repair once Ni atoms traverse through.

Notably, Ni's high chemical affinity to carbon is central to enabling this mechanism. Ni adatoms bind strongly to graphene, so much so that they can even form a carbide-like surface compound at merely ~100 °C on Ni(111).[51] First-principles studies have demonstrated significant charge transfer from Ni to graphene, indicating a strong Ni–C interaction.[49] This strong interaction can locally weaken the graphene lattice when a Ni adatom is adsorbed, facilitating the breaking of a C–C bond or the transient release of a carbon atom. In essence, a Ni cluster or adatom anchored on graphene creates a transient atomic-scale defect through which Ni can inject into the underlying interface. Upon annealing to 900 K, Ni atoms diffuse to the Gr/Ir interface one by one and then bind to the Ir surface underneath. Once positioned beneath graphene, the Ni atoms become stabilized through bonding with the Ir substrate, and the graphene layer reconstructs to restore its continuity, as reflected by the nearly perfect moiré observed after intercalation. The exchange-mediated route is consistent with prior reports. For instance, on Gr/Ru(0001), Si penetrates via a transient Si–C exchange followed by graphene self-healing.[52] Strong C-binding metals (e.g., Ni, Fe) can permeate graphene without pre-existing vacancies, whereas weakly interacting species (e.g., Pb) intercalate primarily at edges or defects. The random spatial distribution of Ni islands beneath an intact graphene monolayer (Figure S5), rather than any directional growth originating from step edges or graphene boundaries, further argues against edge-mediated diffusion. Instead, the observed islands morphology and spatial placement, combined with literature on exchange intercalation, suggest that Ni intercalation in Gr/Ir(111) proceeds via point-defects or exchange mechanisms rather than through edge diffusion.

Finally, we examined the stability of the intercalated Ni layer at elevated temperatures. The Gr/Ni/Ir sample was annealed stepwise up to 1500 K (Figure S7). Following these high-temperature treatments, the graphene moiré remained clearly visible with inverted contrast relative to pristine Gr/Ir(111), while retaining its characteristic periodicity. These results indicate that at 1500 K, the efficiency of Ni intercalation beneath graphene on Ir(111) declines markedly compared to

900 K. This behavior suggests that, with rising temperature, a fraction of Ni atoms either desorbs from the surface or diffuses toward step edges, as evidenced by the appearance of diffusive step edges and the accumulation of bright clusters along the step edges (Figure S7). Such features are not observed in other STM scans of graphene on Ir(111).

Conclusions

In summary, we studied Ni nanocluster nucleation, growth, and intercalation on the graphene moiré on Ir(111) using STM. At room temperature, Ni preferentially nucleates at fcc sites, forming well-defined triangular islands through anisotropic growth directed by the moiré pattern. The resulting cluster morphology depends on the growth mode, i.e. continuous or stepwise; however, in both cases, Ni forms 3D nanoconfined islands rather than fully wetting the surface. Annealing to ~900 K led to intercalation of a single Ni layer between graphene and Ir(111) while preserving the moiré periodicity, consistent with pseudomorphic growth. The intercalated islands are randomly distributed beneath the graphene layer and are likely formed through a carbon-metal atom exchange mechanism. Two distinct moiré patterns, “round” and “clover-like” were observed, corresponding to intercalation at different preferred registry sites (hcp, fcc, and atop). Collectively, these findings elucidate the mechanism of registry-controlled growth and demonstrate a viable route for fabricating low-roughness interfaces, a key step toward scalable device applications.

Author contributions

S. C.: investigation, methodology, formal analysis, writing – original draft; B. S. A. G., A. O., L. L.: review & editing; M. T.: methodology, review & editing, funding acquisition; N. J.: review & editing, funding acquisition, supervision, project administration. All authors have read and agreed to the published version of the manuscript.

Conflicts of interest

The authors declare no conflict of interest.

Data availability

The data supporting this article have been included as part of the supplementary information (SI). Supplementary information is available. See DOI:

Acknowledgements

N. J., S. C., and L. L. acknowledge support from the National Science Foundation (NSF) DMR-2211474. M. T., B. S. A. G., and A. O. acknowledge support from the NSF CHE-2102622.

References

View Article Online
DOI: 10.1039/D6NR00871B

1 W. P. Halperin, *Rev. Mod. Phys.*, 1986, **58**, 533–606.
2 K.-H. Meiwes-Broer, *Metal Clusters at Surfaces*, Springer Berlin Heidelberg, Berlin, Heidelberg, 1st edn., 2000.
3 H.-G. Boyen, G. Kästle, F. Weigl, B. Koslowski, C. Dietrich, P. Ziemann, J. P. Spatz, S. Riethmüller, C. Hartmann, M. Möller, G. Schmid, M. G. Garnier and P. Oelhafen, *Science*, 2002, **297**, 1533–1536.
4 K. S. Novoselov, A. K. Geim, S. V. Morozov, D. Jiang, Y. Zhang, S. V. Dubonos, I. V. Grigorieva and A. A. Firsov, *Science*, 2004, **306**, 666–669.
5 S. Jia-Tao, D. Shi-Xuan, X. Wen-De, H. Hao, Z. Yu-Yang, L. Guo and G. Hong-Jun, *Chin. Phys. B*, 2009, **18**, 3008–3013.
6 M. P. Fanti, *Lecture Notes in Electrical Engineering*, 2011, **85**, 3–13.
7 D. Iaia, A. Kubetzka, K. von Bergmann and R. Wiesendanger, *Phys. Rev. B*, 2016, **93**, 134409.
8 J. Chen, B. Lim, E. P. Lee and Y. Xia, *Nano Today*, 2009, **4**, 81–95.
9 M. Batzill, *Surf. Sci. Rep.*, 2012, **67**, 83–115.
10 F. Ruffino and F. Giannazzo, *Crystals*, 2017, **7**, 219.
11 A. B. Preobrajenski, M. L. Ng, A. S. Vinogradov and N. Mårtensson, *Phys. Rev. B*, 2008, **78**, 073401.
12 T. A. Land, T. Michely, R. J. Behm, J. C. Hemminger and G. Comsa, *Surf. Sci.*, 1992, **264**, 261–270.
13 M. Sicot, S. Bouvron, O. Zander, U. Rüdiger, Yu. S. Dedkov and M. Fonin, *Appl. Phys. Lett.*, 2010, **96**, 093115.
14 A. L. Vázquez de Parga, F. Calleja, B. Borca, M. C. G. Passeggi, J. J. Hinarejos, F. Guinea and R. Miranda, *Phys. Rev. Lett.*, 2008, **100**, 056807.
15 S. Marchini, S. Günther and J. Wintterlin, *Phys. Rev. B*, 2007, **76**, 075429.
16 S. J. Altenburg, M. Lattelais, B. Wang, M.-L. Bocquet and R. Berndt, *J. Am. Chem. Soc.*, 2015, **137**, 9452–9458.
17 J. Coraux, A. T. N'Diaye, C. Busse and T. Michely, *Nano Lett.*, 2008, **8**, 565–570.
18 A. T. N'Diaye, J. Coraux, T. N. Plasa, C. Busse and T. Michely, *New J. Phys.*, 2008, **10**, 043033.
19 A. T. N'Diaye, S. Bleikamp, P. J. Feibelman and T. Michely, *Phys. Rev. Lett.*, 2006, **97**, 215501.
20 A. T. N'Diaye, T. Gerber, C. Busse, J. Myslivečeк, J. Coraux and T. Michely, *New J. Phys.*, 2009, **11**, 103045.
21 Y. Pan, M. Gao, L. Huang, F. Liu and H.-J. Gao, *Appl. Phys. Lett.*, 2009, **95**, 093106.
22 L. Li, Y. Wang, L. Meng, R. T. Wu and H. J. Gao, *Appl. Phys. Lett.*, 2013, **102**, 093106.
23 R. C. de Campos Ferreira, L. H. de Lima, L. Barreto, C. C. Silva, R. Landers and A. de Siervo, *Chem. Mater.*, 2018, **30**, 7201–7210.
24 M. Sicot, Y. Fagot-Revurat, B. Kierren, G. Vasseur and D. Malterre, *Appl. Phys. Lett.*, 2014, **105**, 191603.
25 L. Jin, Q. Fu, Y. Yang and X. Bao, *Surf. Sci.*, 2013, **617**, 81–86.
26 I. Horcas, R. Fernández, J. M. Gómez-Rodríguez, J. Colchero, J. Gómez-Herrero and A. M. Baro, *Rev. Sci. Instrum.*, 2007, **78**, 013705.
27 B. S. A. Gedara and M. Trenary, *J. Vac. Sci. Technol. B*, 2024, **42**, 014201.
28 K. Donner and P. Jakob, *J. Chem. Phys.*, 2009, **131**, 164701.

View Article Online
DOI: 10.1039/D6NR00871B

29 Q. Zhou, Y. Du, L. Zhang and D. Yi, *J. Phys. Chem. C*, 2024, **128**, 968–973.
30 Y. Du, D. Yi and X. Wang, *Carbon*, 2022, **192**, 295–300.
31 L. Zhang, J. Zhang, X. Duan and D. Yi, *Small*, 2025, **21**, e04999.
32 M. T. Hershberger, M. Hupalo, P. A. Thiel and M. C. Tringides, *J. Phys.: Condens. Matter*, 2013, **25**, 225005.
33 J. Krug, P. Politi and T. Michely, *Phys. Rev. B*, 2000, **61**, 14037–14046.
34 J. Halle, N. Néel and J. Kröger, *J. Phys. Chem. C*, 2016, **120**, 5067–5073.
35 S. L. Kovalenko, B. V. Andryushechkin and K. N. Eltsov, *Carbon*, 2020, **164**, 198–206.
36 G. Li, H. Zhou, L. Pan, Y. Zhang, L. Huang, W. Xu, S. Du, M. Ouyang, A. C. Ferrari and H.-J. Gao, *J. Am. Chem. Soc.*, 2015, **137**, 7099–7103.
37 E. Gråsäs, J. Knudsen, U. A. Schröder, T. Gerber, C. Busse, M. A. Arman, K. Schulte, J. N. Andersen and T. Michely, *ACS Nano*, 2012, **6**, 9951–9963.
38 E. Starodub, N. C. Bartelt and K. F. McCarty, *J. Am. Chem. Soc.*, 2010, **132**, 8175–8179.
39 P. Sutter, P. Albrecht, X. Tong and E. Sutter, *J. Phys. Chem. C*, 2013, **117**, 6320–6324.
40 L. Bignardi, P. Lacovig, M. M. Dalmiglio, F. Orlando, A. Ghafari, L. Petaccia, A. Baraldi, R. Larciprete and S. Lizzit, *2D Mater.*, 2017, **4**, 025106.
41 S. Vlaic, A. Kimouche, J. Coraux, B. Santos, A. Locatelli and N. Rougemaille, *Appl. Phys. Lett.*, 2014, **104**, 101602.
42 M. Sicot, P. Leicht, A. Zusan, S. Bouvron, O. Zander, M. Weser, Y. S. Dedkov, K. Horn and M. Fonin, *ACS Nano*, 2012, **6**, 151–158.
43 M. Petrović, I. Šrut Rakić, S. Runte, C. Busse, J. T. Sadowski, P. Lazić, I. Pletikosić, Z.-H. Pan, M. Milun, P. Pervan, N. Atodiresei, R. Brako, D. Šokčević, T. Valla, T. Michely and M. Kralj, *Nat. Commun.*, 2013, **4**, 2772.
44 J. Kwak, S.-Y. Kim, Y. Jo, N. Y. Kim, S. Y. Kim, Z. Lee and S.-Y. Kwon, *Adv. Mater.*, 2018, **30**, 1800022.
45 S. C. O'Hern, M. S. H. Boutilier, J. C. Idrobo, Y. Song, J. Kong, T. Laoui, M. Atieh and R. Karnik, *Nano Lett.*, 2014, **14**, 1234–1241.
46 Y. Pan, H. G. Zhang, D. X. Shi, J. T. Sun, S. X. Du, F. Liu and H.-J. Gao, *Adv. Mater.*, 2009, **21**, 2777–2780.
47 C. Romero-Muñiz, A. Martín-Recio, P. Pou, J. M. Gómez-Rodríguez and R. Pérez, *Phys. Chem. Chem. Phys.*, 2018, **20**, 13370–13378.
48 Y. Cui, J. Gao, L. Jin, J. Zhao, D. Tan, Q. Fu and X. Bao, *Nano Res.*, 2012, **5**, 352–360.
49 X. Liu, C. Z. Wang, M. Hupalo, W. C. Lu, M. C. Tringides, Y. X. Yao and K. M. Ho, *Phys. Chem. Chem. Phys.*, 2012, **14**, 9157–9166.
50 P. Zhao, P. Ren, C. J. K. J. Weststrate, Y. Xu, D. B. Cao, H. Xiang, J. Xu, Y. Yang, Y. W. Li, J. W. H. Niemantsverdriet, X. Wen and X. Yu, *J. Phys. Chem. C*, 2018, **122**, 22903–22910.
51 J. Lahiri and M. Batzill, *Appl. Phys. Lett.*, 2010, **97**, 023102.
52 L. Meng, R. Wu, H. Zhou, G. Li, Y. Zhang, L. Li, Y. Wang and H. J. Gao, *Appl. Phys. Lett.*, 2012, **100**, 083101.

View Article Online
DOI: 10.1039/D6NR00871B

Data availability

The data supporting this article have been included as part of the supplementary information (SI). Supplementary information is available. See DOI: